Journal of Materials Chemistry C

ROYAL SOCIETY OF CHEMISTRY

COMMUNICATION

View Article Online
View Journal | View Issue

Cite this: J. Mater. Chem. C, 2023, 11, 5018

Received 13th February 2023,
Accepted 12th March 2023

DOI: 10.1039/d3tc00523b

rsc.li/materials-c

Tuning white light emission and band gap in the one-dimensional metal halide $(C_6H_{13}N_4)_3Pb_2Br_7$ by pressure engineering†

Nan Li,[a] Yuanyuan Fang,[a] Long Zhang, *[a] Kai Wang [ab] and Bo Zou *[a]

One-dimensional (1D) metal halides have become promising white-light-emitting materials because of their unique broadband emission. Understanding the relationship between the optical characteristics and crystal structures of 1D metal halides is crucial to advancing their applications in the optoelectronic field. Here, we reported the pressure-driven optical and structural responses of the 1D metal halide $(HMTA)_3Pb_2Br_7$ (HMTA = hexamethylenetetramine, $C_6H_{13}N_4^+$, cations). The broadband emission enhancement was achieved by applying mild pressure (<0.6 GPa), accompanied by a prolongation of the carrier lifetime. Moreover, the band gap narrowed with pressure, which was attributed to the enhanced orbital coupling between the metal and halogen by lattice contraction. Our high-pressure studies not only reveal the regulation mechanism of the self-trapped exciton (STE) emission in 1D metal halides but also indicate that pressure treatment can serve as a powerful strategy to tune the emission of white-light materials.

Metal halides have many unique advantages, such as a tunable crystal structure and extraordinary optical properties, making them potential optoelectronic materials.[1–7] Organic metal halides with low dimensionality can be obtained by the co-crystallization of organic amines and metal halides, in which large organic cations serve as spacers.[8–11] Given the separation of building blocks in low-dimensional metal halides, they display the inherent characteristics of single building blocks. Low-dimensional metal halides can show pure white broadband emission covering the whole visible spectra with a high photoluminescence quantum yield, which are expected to become the forthcoming generation of solid-state illumination candidates.[12–16] Considering the quantum confinement and strong electron–phonon coupling, self-trapped excitons (STEs) are widely assumed to be responsible for broadband emission.[17–21] However, the efficient emission of low-dimensional metal halides under ambient conditions is not yet ideal because of suboptimal electron–phonon coupling strength. In implementing the efficient broadband emission of low-dimensional metal halides, it is necessary to enhance the understanding of the structure–property relationships.

Pressure, as a clean and powerful tool, can validly tune the optical properties and crystal structure of functional materials, which enables numerous intriguing physical phenomena.[22–24] In low-dimensional metal halides, the regulation of various physicochemical properties including structural phase transition, band gap narrowing, metallization, and photoluminescence (PL) enhancement has been achieved by high-pressure engineering.[25–32] In two-dimensional (2D) $(HA)_2(GA)Pb_2I_7$, the trapping ability of the carrier is suppressed to produce a significant pressure-induced PL enhancement.[31] 1D $CsCu_2I_3$ can generate new defect-related localized exciton emission by pressure-induced crystal structure phase transition.[32] Zero-dimensional (0D) $Cs_3Bi_2I_9$ exhibits band gap narrowing and pressure-induced metallization.[27] High-pressure technology provides a comprehensive understanding of the dynamic mechanism at the atomic level of matter, and it has shown great application potential in material modification.[33,34]

Herein, we systematically study the optical characteristics and the structural responses of the 1D metal halide $(HMTA)_3Pb_2Br_7$ by *in situ* high-pressure characterization methods. By carrying out high-pressure PL, ultraviolet-visible (UV-vis) absorption, synchrotron X-ray diffraction, Raman experiments, and first-principle calculations, we have achieved the precise modulation of the broadband white-light emission and optical band gap in 1D $(HMTA)_3Pb_2Br_7$ (HMTA = hexamethylenetetramine, $C_6H_{13}N_4^+$, cations), accompanied by its lattice shrinkage. Our research elaborates on the relationship between the lattice shrinkage and optical characteristics of materials and presents the view for understanding low-dimensional metal halides concomitantly.

In situ high-pressure optical micrographs and PL experiments were performed to study the changes in the emission

[a] State Key Laboratory of Superhard Materials, College of Physics, Jilin University, Changchun 130012, P. R. China. E-mail: zhanglong@jlu.edu.cn, zoubo@jlu.edu.cn
[b] Shandong Key Laboratory of Optical Communication Science and Technology, School of Physics Science and Information Technology, Liaocheng University, Liaocheng 252000, China

† Electronic supplementary information (ESI) available. See DOI: https://doi.org/10.1039/d3tc00523b

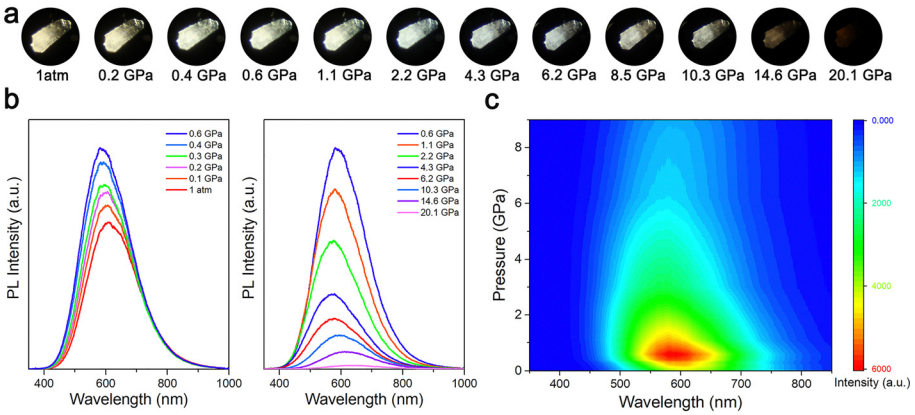

Fig. 1 (a) High-pressure optical PL micrographs of the $(HMTA)_3Pb_2Br_7$ crystal. (b) PL spectra of the $(HMTA)_3Pb_2Br_7$ crystal measured under different pressures. (c) Two-dimensional projection of the PL spectra under high pressure.

behavior of $(HMTA)_3Pb_2Br_7$. Fig. 1 shows the emission properties of $(HMTA)_3Pb_2Br_7$ as a function of pressure. Under ambient conditions, the $(HMTA)_3Pb_2Br_7$ crystal showed a yellowish-white broadband emission centered at 611 nm with a large full width at half maximum (FWHM) of 190 nm, which was attributable to STE radiation recombination.[35] With the increase of pressure, the emission of $(HMTA)_3Pb_2Br_7$ was gradually enhanced until reaching a mild pressure of 0.6 GPa. Upon further compression, the emission intensity started to weaken, and it was nearly quenched until the pressure reached 20.1 GPa (Fig. 1b). In addition, the pressure effects on the emission intensity (Fig. S3a, ESI†) and the position of the PL peak (Fig. S3b, ESI†) were recorded for $(HMTA)_3Pb_2Br_7$, which intuitively shows the variation of the PL. The PL peaks exhibited a blue shift before 5.0 GPa, followed by a red shift upon further compression. The PL photographs of the $(HMTA)_3Pb_2Br_7$ single crystal exhibited color changes from yellowish-white to white as a function of pressure (Fig. 1a). In addition, we described the evolutionary trend of the color rendering index (CRI) and correlated color temperature (CCT) with pressure (Fig. S4, ESI†). The CCT at 1 atm is 2671 K with a CRI of 79, which is defined as "warm" white light. With the increase of pressure, the CRI initially decreases before reaching 5.0 GPa and then gradually increases. The CCT attains modulation from warm white light to natural white light. Therefore, high pressure can not only increase emission intensity but also adjust emission chromaticity. Fig. 1c shows the pressure-induced 2D projection of the emission spectra, demonstrating coordinated variations in emission peak location and intensity. The emission is reversible after decompression, which demonstrates a strong memory effect of the crystal structure with soft organic cations (Fig. S5, ESI†).[36] Pressure-induced broadband emission enhancement stemming from exciton self-trapping was achieved in various low-dimensional metal halide perovskites, which have a common feature. That is, a structural phase transition with reduced symmetry is necessary for the activation of efficient broadband emission by increasing inorganic octahedral distortion and electron–phonon coupling strength, which leads to the formation of stable STEs with enhanced optical activity (Table S1, ESI†). Therefore, the continuous regulation of the STE properties of low-dimensional metal halides under mild pressure is conducive to promoting the application and use of chemical strain replacement under practical conditions.

The band gap changes of the material can reflect variations in orbital coupling between the metal and halogen at high pressure. Hence, we carried out UV-vis absorption experiments to study the pressure effects on the band gap for the $(HMTA)_3Pb_2Br_7$ single crystal (Fig. 2). As shown in Fig. 2a, the absorption edge was located at 397 nm under ambient conditions. The absorption edge manifests a sustained red shift from an initial 397 nm to 459 nm at 20.3 GPa, corresponding to large band gap narrowing. The band gap was evaluated from the Tauc plot by plotting $(\alpha h\nu)^2$ *versus* $h\nu$ to extrapolate the intercept with the energy axis. The band gap of $(HMTA)_3Pb_2Br_7$ is 3.12 eV at 1 atm (Fig. 2b). The band gap undergoes narrowing from the initial value of 3.12 eV to 2.70 eV at 20.3 GPa (Fig. 2c), which indicates the flexible band gap tunability of the 1D metal halide $(HMTA)_3Pb_2Br_7$ by pressure engineering.

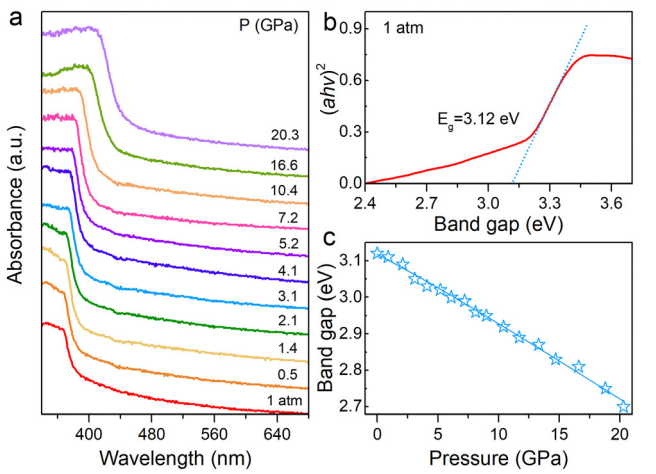

Fig. 2 (a) Evolution of the UV-Vis absorption spectra of the $(HMTA)_3Pb_2Br_7$ crystal at selected pressures. (b) The Tauc plot of $(HMTA)_3Pb_2Br_7$ under ambient conditions. (c) Demonstration of the band-gap narrowing in $(HMTA)_3Pb_2Br_7$ at high pressures.

To investigate PL decay dynamics, high-pressure time-resolved PL measurements of $(HMTA)_3Pb_2Br_7$ were performed at different pressures (Fig. S6, ESI†). A double exponential function was used to fit the decay curves. The double exponential corresponds to two decay channels, where the fast decay component τ_1 and the slow decay component τ_2 refer to the recombination of STEs.[35] During the compression process, the lifetime first becomes longer before reaching 0.6 GPa and then gradually shortens until 20.0 GPa (Table S2, ESI†). Notably, the pressure to obtain the maximum lifetime is consistent with the pressure to obtain the maximum emission strength. We further calculated the evolution of the average PL lifetime for $(HMTA)_3Pb_2Br_7$ under high pressure. With the increase of the applied pressure, the average PL lifetime becomes longer before reaching 0.6 GPa, indicating that more STEs are trapped by distorted $Pb_2Br_9^{5-}$ dimers.[37] The trap-assisted exciton radiative process can enhance PL emission. When the pressure exceeds 0.6 GPa, the average PL lifetime begins to shorten. The high-pressure decay kinetics further deepen the physical understanding of the pressure effect on the optical properties of $(HMTA)_3Pb_2Br_7$.

Optical responses under high pressure depend on structural changes. We carried out high-pressure angle-dispersive X-ray diffraction (ADXRD) and Raman measurements to comprehensively understand the relationship between the crystal structure and physicochemical properties of $(HMTA)_3Pb_2Br_7$. At ambient pressure, $(HMTA)_3Pb_2Br_7$ has a hexagonal crystal structure with a space group of $P6_3/m$, which is well consistent with previous reports (Fig. S7, ESI†).[35] The left panel of Fig. 3b exhibits arrays of organic metal halides, with an individual inorganic unit (Fig. 3b, middle panel). The upper and lower right panels of Fig. 3b show the face-sharing lead bromide dimers $[Pb_2Br_9]^{5-}$ and HMTA cation $C_6H_{13}N_4^+$, respectively. Fig. 3a displays the ADXRD patterns at different pressures. The diffraction peaks shifted to higher diffraction angles with the application of pressure. During the compression process, no diffraction peaks appeared and disappeared, which indicated the continuous shrinkage of the lattice with constant symmetry. In addition, $(HMTA)_3Pb_2Br_7$ did not show amorphization under high pressure and the main diffraction peaks still existed, although the pressure reached 20.0 GPa, indicating a stable structure. The diffraction peaks recovered to their initial positions as the pressure returned to 1 atm, showing that the changes in the crystal structure were reversible, which was consistent with the reversibility of optical properties (Fig. S8, ESI†). High-pressure Raman spectra are shown in Fig. S9 (ESI†), and no phase transition was observed as pressure increased, which further supported the results of ADXRD.

Fig. 3c shows the pressure-induced evolution of lattice parameters for $(HMTA)_3Pb_2Br_7$. Under ambient conditions, the cell parameters of $(HMTA)_3Pb_2Br_7$ are a = 24.51 Å and c = 9.79 Å. The cell parameters gradually decreased with increasing pressure, indicating that the lattice axes were compressed. High-pressure compressibility can be regarded as a parameter to evaluate the pressure sensitivity and the capacity of the structure to contract in a specific direction.[38] Fig. S10 (ESI†) shows the compressibility of the a and c axes of $(HMTA)_3Pb_2Br_7$ at different pressures. During the compression process, the compressibility decreased with the increase of pressure because of more compact structures at high pressure. Notably, the compressibility of the a-axis was lower than that of the c-axis, which indicated that the c-axis is more susceptible than the

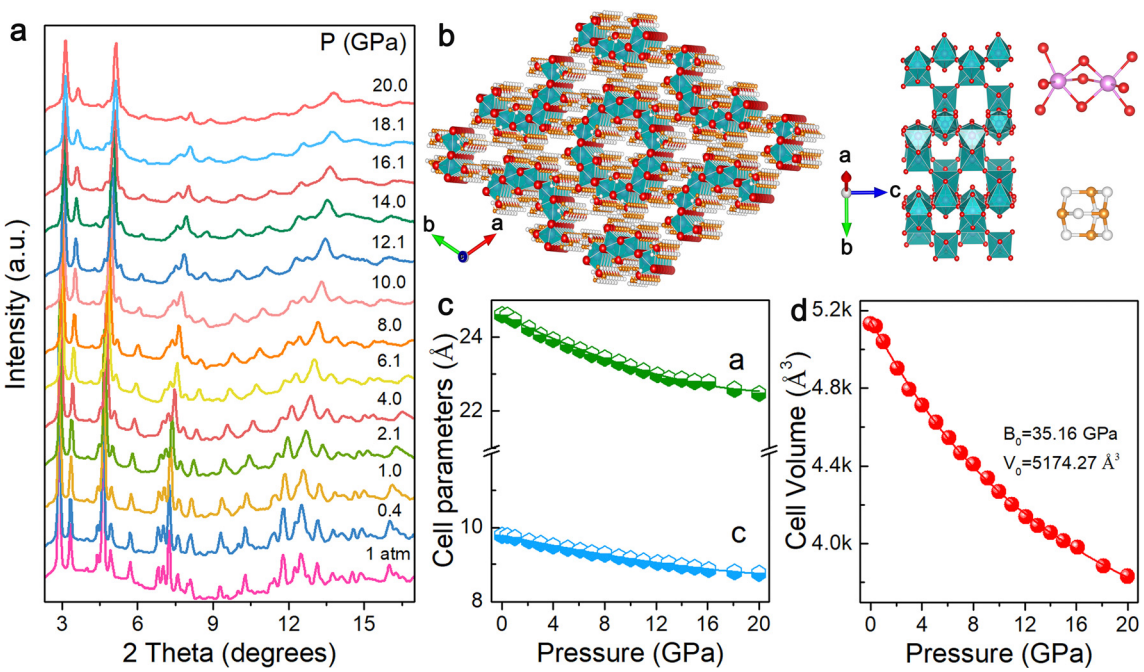

Fig. 3 (a) ADXRD spectra at different pressures. (b) Crystal structure of $(HMTA)_3Pb_2Br_7$. (Magenta: Pb; red: Br; orange: N; white: C; turquoise polyhedra: $PbBr_6$ octahedra and Pb_2Br_9 dimers; H atoms have been omitted.) (c) The changes in cell parameters upon compression. (d) Pressure-dependent evolution of unit-cell volumes.

a-axis to pressure, showing intriguing mechanical anisotropy derived from the unique tubular structure of $(HMTA)_3Pb_2Br_7$. Fig. 3d displays the variations in the volume of the cell unit upon compression. The cell volume continuously shrank with the increase of pressure, confirming that no phase transition occurred. The bulk modulus is 35.16 GPa by fitting the pressure-dependent unit-cell volume to the third-order Birch–Murnaghan equation of state, indicating relatively low compressibility compared with three-dimensional (3D) organic–inorganic hybrid perovskite materials (Table S3, ESI†), which offered a great way to modify optical properties in a large pressure range.

To obtain an in-depth understanding of the electronic structure and optical response of $(HMTA)_3Pb_2Br_7$, we carried out first-principles calculations on the band structures. Fig. 4a depicts the calculated band structures, which show a direct band gap of 2.84 eV for $(HMTA)_3Pb_2Br_7$ at atmospheric pressure. Given the organic molecules located at the deep energy level, the band edge is mainly derived from the inorganic $PbBr_6$ octahedral framework. The valence band maximum is mainly formed by Pb 6s orbitals and Br 4p orbitals, whereas the conduction band minimum is dominated by Pb 6p states, which can be observed from the density of states diagrams. Fig. 4b shows the variation trends of the calculated band gap under high pressure. The band gap narrows gradually during the compression process, which is consistent with the changing trend in the experiment.

The Pb–Br skeleton of metal halides has a great impact on optical characteristics.[39] Fig. 4c and Table S4 (ESI†) show the pressure-dependent Pb–Br bond lengths and Br–Pb–Br bond angles for $(HMTA)_3Pb_2Br_7$, which verify the reason for the band gap reduction during compression. As observed, the Pb–Br bond lengths continuously decreased and the Br–Pb–Br bond angles showed small changes with increasing pressure. In addition, the adjacent $[Pb_2Br_9]^{5-}$ dimers became closer, leading to an enhancement of the electrostatic interaction. These variations will reinforce the overlap of Pb and Br orbital electron clouds, enhancing the electronic band dispersion.[37,40,41] The decreased Pb–Br bond length and Br–Pb–Br bond angle increase the coupling of Pb 6s and Br 4p orbitals at the VBM. The increase of the VBM changes the energy level, resulting in a reduction of the band gap during the compression process (Fig. 4d and e).

The broadband STE emission with a significant Stokes shift is related to inorganic lattice distortion and electron–phonon coupling.[42–44] Here, we discuss the photophysical mechanism of $(HMTA)_3Pb_2Br_7$ under high pressure. Pressure can modulate the inorganic lattice of $(HMTA)_3Pb_2Br_7$, thereby regulating electron–phonon coupling. Under ambient conditions, the broadband STE emission of $(HMTA)_3Pb_2Br_7$ is mainly dominated by the inorganic unit $[Pb_2Br_9]^{5-}$ dimers. Based on our high-pressure PL and absorption experiments, we evaluated the pressure-dependent FWHM and Stokes shift of $(HMTA)_3Pb_2Br_7$. We found that the FWHM of $(HMTA)_3Pb_2Br_7$ crystals showed a decreasing trend before reaching a mild pressure (<1.0 GPa) and subsequently increased in the higher pressure region (Fig. S11a, ESI†). With the increase of pressure, the Stokes shift of $(HMTA)_3Pb_2Br_7$ decreases (Fig. S11b, ESI†), indicating the decreased electron–phonon coupling strength upon compression,

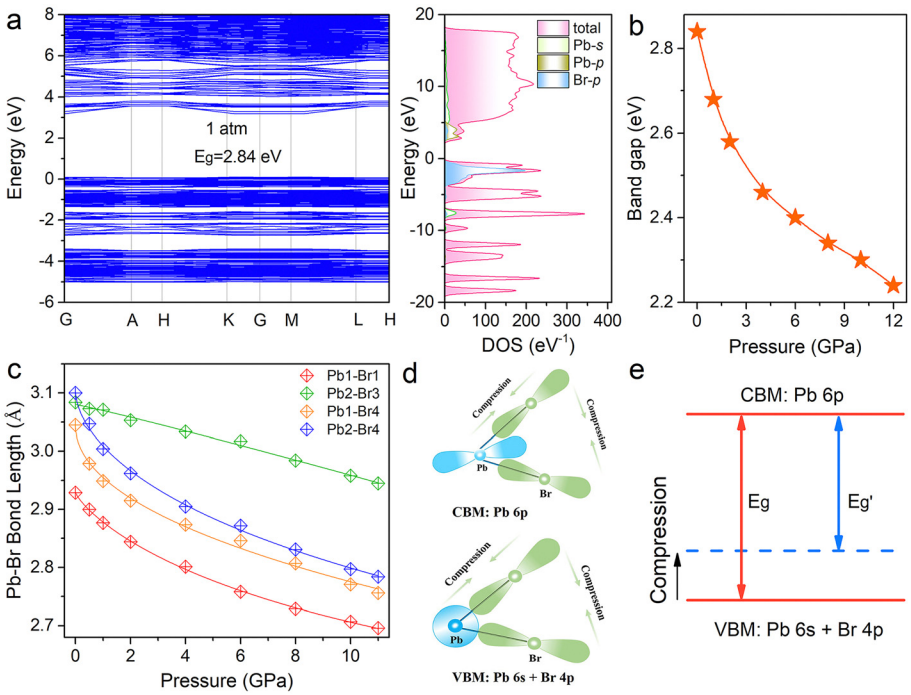

Fig. 4 (a) DFT calculated band structures and projected density of states (DOS) of $(HMTA)_3Pb_2Br_7$ under ambient conditions. (b) Calculated band gap evolution of $(HMTA)_3Pb_2Br_7$ under high pressure. (c) Calculated Pb–Br bond length evolution as a function of pressure. (d) Models of band gap narrowing upon compression. (e) Diagram of the VBM and CBM evolution upon compression.

thereby suppressing the non-radiative transition and enhancing the broadband emission in the low-pressure region.

In summary, the pressure subtly modulates the broadband STE emission of the 1D metal halide $(HMTA)_3Pb_2Br_7$ and elaborates the source of the regulation of STE emission and band gap properties. The pressure-induced lattice contraction of the inorganic unit $[Pb_2Br_9]^{5-}$ dimers effectively decreases the electron–phonon coupling, thereby reducing the non-radiative transition and enhancing the emission, accompanied by the regulation of CCT. Meanwhile, we have achieved pressure-induced band gap narrowing. This work offered a comprehensive understanding of the structure and luminescence characteristics of 1D metal halides and an effective method for regulating electron–phonon coupling in various low-dimensional metal halide materials.

Conflicts of interest

There are no conflicts to declare.

Acknowledgements

This work was supported by the National Natural Science Foundation of China (NSFC) (No. 12204189, 21725304, and 12174146), the Special Construction Project Fund for Shandong Province Taishan Scholars, the China Postdoctoral Science Foundation (No. 2021M691221) and the Fundamental Research Funds for the Central Universities. ADXRD experiments were performed at the 4W2 beamline in Beijing Synchrotron Radiation Facility (BSRF).

References

1 A. Kojima, K. Teshima, Y. Shirai and T. Miyasaka, *J. Am. Chem. Soc.*, 2009, **131**, 6050–6051.
2 X. Hu, X. Zhang, L. Liang, J. Bao, S. Li, W. Yang and Y. Xie, *Adv. Funct. Mater.*, 2014, **24**, 7373–7380.
3 G. Grancini and M. K. Nazeeruddin, *Nat. Rev. Mater.*, 2019, **4**, 4–22.
4 K. Liu, Y. Jiang, Y. Jiang, Y. Guo, Y. Liu and E. Nakamura, *J. Am. Chem. Soc.*, 2019, **141**(4), 1406–1414.
5 L. N. Quan, F. P. G. De Arquer, R. P. Sabatini and E. H. Sargent, *Adv. Mater.*, 2018, **30**, 1801996.
6 C.-H. Lee, N. D. Orloff, T. Birol, Y. Zhu, V. Goian, E. Rocas, R. Haislmaier, E. Vlahos, J. A. Mundy, L. F. Kourkoutis, Y. Nie, M. D. Biegalski, J. Zhang, M. Bernhagen, N. A. Benedek, Y. Kim, J. D. Brock, R. Uecker, X. X. Xi, V. Gopalan, D. Nuzhnyy, S. Kamba, D. A. Muller, I. Takeuchi, J. C. Booth, C. J. Fennie and D. G. Schlom, *Nature*, 2013, **502**, 532–536.
7 M. B. Johnston and L. M. Herz, *Acc. Chem. Res.*, 2016, **49**, 146–154.
8 S. Wang, D. B. Mitzi, C. A. Feild and A. Guloy, *J. Am. Chem. Soc.*, 1995, **117**, 5297–5302.
9 Z. Yuan, C. Zhou, Y. Tian, Y. Shu, J. Messier, J. C. Wang, L. J. van de Burgt, K. Kountouriotis, Y. Xin, E. Holt, K. Schanze, R. Clark, T. Siegrist and B. Ma, *Nat. Commun.*, 2017, **8**, 14051.
10 P. Gao, A. R. Bin Mohd Yusoff and M. K. Nazeeruddin, *Nat. Commun.*, 2018, **9**, 5028.
11 L. Gan, H. He, S. Li, J. Li and Z. Ye, *J. Mater. Chem. C*, 2016, **4**, 10198–10204.
12 L. Zhou, J.-F. Liao and D.-B. Kuang, *Adv. Opt. Mater.*, 2021, **9**, 2100544.
13 B.-B. Su and Z.-G. Xia, *Chin. J. Lumin.*, 2021, **42**, 733–754.
14 M. Z. Rahaman, S. Ge, C.-H. Lin, Y. Cui and T. Wu, *Small Struct.*, 2021, **2**, 2000062.
15 Y. Han, S.-J. Yue and B.-B. Cui, *Adv. Sci.*, 2021, **8**, 2004805.
16 H. Peng, Y. Tian, X. Wang, T. Huang, Z. Yu, Y. Zhao, T. Dong, J. Wang and B. Zou, *ACS Appl. Mater. Interfaces*, 2022, **14**, 12395–12403.
17 E. R. Dohner, E. T. Hoke and H. I. Karunadasa, *J. Am. Chem. Soc.*, 2014, **136**, 1718–1721.
18 D. Cortecchia, J. Yin, A. Bruno, S.-Z. A. Lo, G. G. Gurzadyan, S. Mhaisalkar, J.-L. Brédas and C. Soci, *J. Mater. Chem. C*, 2017, **5**, 2771–2780.
19 D. Cortecchia, S. Neutzner, A. R. Srimath Kandada, E. Mosconi, D. Meggiolaro, F. De Angelis, C. Soci and A. Petrozza, *J. Am. Chem. Soc.*, 2017, **139**, 39–42.
20 B.-B. Cui, Y. Han, B. Huang, Y. Zhao, X. Wu, L. Liu, G. Cao, Q. Du, N. Liu, W. Zou, M. Sun, L. Wang, X. Liu, J. Wang, H. Zhou and Q. Chen, *Nat. Commun.*, 2019, **10**, 5190.
21 D. Cortecchia, J. Yin, A. Petrozza and C. Soci, *J. Mater. Chem. C*, 2019, **7**, 4956–4969.
22 G. Liu, L. Kong, W. Yang and H.-K. Mao, *Mater. Today*, 2019, **27**, 91–106.
23 X. Lü, Y. Wang, C. C. Stoumpos, Q. Hu, X. Guo, H. Chen, L. Yang, J. S. Smith, W. Yang, Y. Zhao, H. Xu, M. G. Kanatzidis and Q. Jia, *Adv. Mater.*, 2016, **28**, 8663–8668.
24 L. Kong, G. Liu, J. Gong, Q. Hu, R. D. Schaller, P. Dera, D. Zhang, Z. Liu, W. Yang, K. Zhu, Y. Tang, C. Wang, S.-H. Wei, T. Xu and H. Mao, *Proc. Natl. Acad. Sci. U. S. A.*, 2016, **113**, 8910–8915.
25 Y. Wang, S. Guo, H. Luo, C. Zhou, H. Lin, X. Ma, Q. Hu, M.-h Du, B. Ma, W. Yang and X. Lü, *J. Am. Chem. Soc.*, 2020, **142**, 16001–16006.
26 Y. Fang, L. Zhang, Y. Yu, X. Yang, K. Wang and B. Zou, *CCS Chem.*, 2021, **2**, 2203–2210.
27 L. Zhang, C. Liu, L. Wang, C. Liu, K. Wang and B. Zou, *Angew. Chem., Int. Ed.*, 2018, **57**, 11213–11217.
28 Y. Yin, W. Tian, H. Luo, Y. Gao, T. Zhao, C. Zhao, J. Leng, Q. Sun, J. Tang, P. Wang, Q. Li, X. Lü, J. Bian and S. Jin, *ACS Energy Lett.*, 2022, **7**, 154–161.
29 Z. Ma, F. Li, D. Zhao, G. Xiao and B. Zou, *CCS Chem.*, 2020, **2**, 71–80.
30 H. Luo, S. Guo, Y. Zhang, K. Bu, H. Lin, Y. Wang, Y. Yin, D. Zhang, S. Jin, W. Zhang, W. Yang, B. Ma and X. Lü, *Adv. Sci.*, 2021, **8**, 2100786.
31 S. Guo, Y. Zhao, K. Bu, Y. Fu, H. Luo, M. Chen, M. P. Hautzinger, Y. Wang, S. Jin, W.-J. Yang and X. Lü, *Angew. Chem., Int. Ed.*, 2020, **132**, 17686–17692.
32 Q. Li, Z. Chen, B. Yang, L. Tan and Z.-W. Quan, *J. Am. Chem. Soc.*, 2020, **142**, 1786–1791.

33 B. Chen, *Matter Radiat. Extremes*, 2020, **5**, 068104.
34 V. V. Atuchin, N. F. Beisel, E. N. Galashov, E. M. Mandrik, M. S. Molokeev, A. P. Yelisseyev, A. A. Yusuf and Z. Xia, *ACS Appl. Mater. Interfaces*, 2015, **7**, 26235–26243.
35 H. Lin, C. Zhou, Y. Tian, T. Besara, J. Neu, T. Siegrist, Y. Zhou, J. Bullock, K. S. Schanze, W. Ming, M.-H. Du and B. Ma, *Chem. Sci.*, 2017, **8**, 8400–8404.
36 Y. Lee, D. B. Mitzi, P. W. Barnes and T. Vogt, *Phys. Rev. B: Condens. Matter Mater. Phys.*, 2003, **68**, 020103.
37 T. Yin, B. Liu, J. Yan, Y. Fang, M. Chen, W. K. Chong, S. Jiang, J.-L. Kuo, J. Fang, P. Liang, S. Wei, K. P. Loh, T. C. Sum, T. J. White and Z. X. Shen, *J. Am. Chem. Soc.*, 2019, **141**, 1235–1241.
38 A. B. Cairns, J. Catafesta, C. Levelut, J. Rouquette, A. van der Lee, L. Peters, A. L. Thompson, V. Dmitriev, J. Haines and A. L. Goodwin, *Nat. Mater.*, 2013, **12**, 212–216.
39 L. Kong, G. Liu, J. Gong, Q. Hu, R. Schaller, P. Dera, D. Zhang, Z. Liu, W. Yang, K. Zhu and H. Mao, *Proc. Natl. Acad. Sci. U. S. A.*, 2016, **113**, 8910–8915.
40 H. Li, Y. Qin, B. Shan, Y. Shen, F. Ersan, E. Soignard, C. Ataca and S. Tongay, *Adv. Mater.*, 2020, **32**, 1907364.
41 E. Mosconi, P. Umari and F. De Angelis, *J. Mater. Chem. A*, 2015, **3**, 9208–9215.
42 A. D. Wright, C. Verdi, R. L. Milot, G. E. Eperon, M. A. Perez-Osorio, H. J. Snaith, F. Giustino, M. B. Johnston and L. M. Herz, *Nat. Commun.*, 2016, **7**, 11755.
43 D. B. Straus, S. Hurtado Parra, N. Iotov, J. Gebhardt, A. M. Rappe, J. E. Subotnik, J. M. Kikkawa and C. R. Kagan, *J. Am. Chem. Soc.*, 2016, **138**, 13798–13801.
44 E. I. Marchenko, V. V. Korolev, S. A. Fateev, A. Mitrofanov, N. N. Eremin, E. A. Goodilin and A. B. Tarasov, *Chem. Mater.*, 2021, **33**, 7518–7526.